Journal of Materials Chemistry A

Accepted Manuscript

ROYAL SOCIETY OF CHEMISTRY

www.rsc.org/materialsA

Pt-MoO_3-RGO Ternary Hybrid Hollow Nanorod Arrays as High-Performance Catalysts for Methanol Electrooxidation

An-Liang Wang,[†] Chao-Lun Liang,[‡] Xue-Feng Lu,[†] Ye-Xiang Tong,[†] and Gao-Ren Li*,[†]

[†]*MOE Laboratory of Bioinorganic and Synthetic Chemistry, KLGHEI of Environment and Energy Chemistry, School of Chemistry and Chemical Engineering, Sun Yat-sen University, Guangzhou 510275, China*

[‡]*Instrumental Analysis and Research Centre, Sun Yat-Sen University, Guangzhou 510275, China*

E-mail: ligaoren@mail.sysu.edu.cn

ABSTRACT

Here we design and synthesize the novel Pt-MoO_3-RGO (reduced graphene oxide) ternary hybrid hollow nanorod arrays (HNRAs) as anode catalysts for methanol electrooxidation. These fabricated Pt-MoO_3-RGO HNRAs own high dispersive MoO_3, RGO, and Pt nanocrystals (~3 nm), which leads to rich heterogeneous interfaces and strong synergistic effects among Pt, MoO_3 and RGO. The Pt-MoO_3-RGO HNRAs exhibit high electrochemically active surface area (ECSA) of 71.20 $m^2 \cdot (g, Pt)^{-1}$, which is much higher than those of Pt-MoO_3 HNRAs (34.23 $m^2 \cdot (g, Pt)^{-1}$) and commercial Pt/C catalysts (52.89 $m^2 \cdot (g, Pt)^{-1}$). Because of the strong synergistic effects and structural advantages, these Pt-MoO_3-RGO HNRAs show much enhanced electrocatalytic activity, durability and CO antipoisoning ability compared with Pt-MoO_3 HNRAs and commercial Pt/C catalysts. Besides, the electrocatalytic activity of Pt-MoO_3-RGO HNRAs alos exceeds many Pt-based catalysts reported in the literature. Our finding demonstrates the importance of the interfacial and structural effects in harnessing the true electrocatalytic potential of Pt-based catalysts and will open up new strategies for the development of high-performance catalysts for methanol electrooxidation.

Keywords: Pt-MoO_3-RGO; hybrid; hollow nanorod array; electrocatalysis; methanol electrooxidation

1. Introduction

Direct methanol fuel cells (DMFCs) have been regarded as promising future power sources, especially for mobile and portable applications.[1-2] The main reactions in the DMFCs include methanol oxidation on anode and oxygen reduction on cathode.[3-8] Among the different catalysts for anode reactions, platinum (Pt) exhibits the highest electrocatalytic activity for methanol oxidation and there is not yet any choice to replace Pt.[9-11] However, with Pt alone as anode catalysts, several obvious disadvantages, such as insufficient activity, unsatisfied durability and high cost, largely limit its wide application in the DMFCs.[12-13] It has been a long-standing challenge to develop the efficient and durable Pt-based electrocatalysts at low cost.[14-15]

Recently many efforts have been devoted to developing strongly coupled Pt/metal oxide hybrid materials for advanced electrocatalysts for DMFCs.[16-19] However, the metal oxides are limited by their intrinsic poor electrical conductivity and the difficulties in achieving morphological stability and accordingly they are hard to maximally promote the performance of Pt electrocatalysts.[20-21] Graphene (or reduced graphene oxide, RGO) as a new generation support also has attracted much interest because of its high electrical conductivity, high surface area, good chemical stability, and strong adhesion to catalyst particles.[22-23] But it is very easy to stack together because of the π-π interactions. As an effective way to improve the electronic conductivity and synergistic effects, the Pt/metal oxide/RGO hybrid catalysts should be proposed.[24] It is expected that the novel Pt/metal oxide/RGO ternary hybrid electrocatalysts with high performance could be designed and fabricated because the multicomponent active sites, particularly Pt-metal oxide and RGO interfaces, will facilitate the activation of reagents to improve catalytic activities. On the other hand, it is essential to design favorable nanostructures of hybrid catalysts so that to reduce undesirable side effects, such as low utilization ratio of catalyst and poor interaction between Pt and electroactive species.[25-26] The following three important issues associated with the design of hybrid electrocatalysts with high performance should be taken into consideration: (*i*) the hybrid catalysts should own high dispersive components so that they have rich heterogeneous interfaces and strong synergistic effects; (*ii*) the hybrid catalysts should have large surface area and well organized porous channels in order to afford more

exposed active sites, which in turn will provide much more effective interactions with active species; (*iii*) the hybrid catalysts should can efficiently resist dissolution, Ostwald ripening, and aggregation of catalysts to maintain high catalytic activity and durability. However, at present, almost no effective method exists for addressing all of above considerations simultaneously.

Based on the above considerations, here the Pt-MoO_3-RGO ternary hybrid hollow nanorod arrays (HNRAs) were designed and synthesized as anode catalysts for DMFCs. It has been well recognized that the one-dimensional (1D) hollow nanostructures are highly favorable for catalysts because the large specific surface area and anisotropic morphology will obviously improve catalyst utilization and mass transport and are much less vulnerable to aggregation, Ostwald ripening and dissolution than nanoparticles.[27-29] However, up to now, there is almost no report on the synthesis of Pt/metal oxide/RGO ternary hybrid HNRAs because of the difficulties involved in controlling growth of the composite nanostructures in the presence of different precursors with various reduction kinetics. Here we successfully fabricate Pt-MoO_3-RGO ternary hybrid HNRAs with high dispersive Pt, MoO_3 and RGO, which own favorable structures and rich heterogeneous interfaces for catalytic reactions.The fabricated Pt-MoO_3-RGO hybrid HNRAs also exhibit obvious electron delocalization among Pt 4*f* orbitals, Mo 3*d* orbitals and RGO π-conjugated ligands and show the strong synergistic effects among Pt, MoO_3 and RGO. The results in this paper prove that the fabricated Pt-MoO_3-RGO hybrid HNRAs show much enhanced electrocatalytic activity and durability compared with Pt-MoO_3 HNRAs and commercial Pt/C catalysts. To the best of our knowledge, this is the first study of methanol electrooxidation on the Pt-MoO_3-RGO ternary hybrid HNRAs.

2. Experimental Section

Synthesis of MoO_3/RGO/Pt hybrid hollow nanorod arrays (HNRAs): All chemical reagents were analytical (AR) grade. Electrodeposition was carried out in a simple three-electrode electrolytic cell via galvanostatic electrolysis. A saturated calomel electrode (SCE) was used as the reference electrode that was connected to the cell with a double salt bridge system. All potentials used in electrodeposition were the values *vs* SCE. The graphite electrode was used as a counter electrode (spectral grade, 1.8 cm^2). A Ti

plate (99.99%, 1.0 cm^2) was used as working electrode, and it was cleaned ultrasonically in 0.1 M HCl, distilled water, and acetone and then rinsed in distilled water again before electrodeposition. The Pt-MoO_3-RGO hybrid HNRAs were fabricated by the procedures described as follows and shown in scheme S1 in supporting information (SI):

(1) ZnO nanorod arrays (NRAs) templates were electrodeposited on Ti substrate in solution of 0.01 M $Zn(NO_3)_2$ +0.05 M NH_4NO_3 at current density of 0.5 $mA \cdot cm^{-2}$ at 70 ^oC for 90 min. SEM image of ZnO NRAs is shown in Figure S1.

(2) The ZnO@MoO_3-Mo-RGO NRAs were fabricated as following: Electrodeposition was first carried out on the surfaces of ZnO NRAs in solution of 0.02 M Na_2MoO_4+8 mg L^{-1} GO+0.8 M Na_2SO_4 +0.02 M CH_3COONH_4+0.02 M Na_2EDTA at current density of 0.75 $mA \cdot cm^{-2}$ at 70 ^oC for 6 min, and then the samples were immersed in solution of 0.05 M H_2PtCl_6 for 10 h. SEM of ZnO@Pt-MoO_3-RGO hybrid NRAs is shown in Figure S2.

(4) Finally Pt-MoO_3-RGO hybrid HNRAs were fabricated by etching ZnO from the ZnO@Pt-MoO_3-RGO NRAs in 0.002 M NaOH solution for 4 h. SEM image of Pt-MoO_3-RGO hybrid HNRAs is shwon in Figure 1a-b.

Structural Characterization: Surface morphologies and microstructures of the fabricated Pt-MoO_3-RGO HNRAs were characterized by field emission scanning electron microscopy (FE-SEM, JSM-6330F) and transmission electron microscope (TEM, JEM-2010HR). The fabricated samples were also characterized by energy-dispersive X-ray spectroscopy (EDX, INCA 300) to determine the compositions. Chemical-state analysis of the samples was carried out by X-ray photoelectron spectroscopy (XPS) using an ESCALAB 250 X-ray photoelectron spectrometer. All XPS spectra were corrected using the C 1s line at 284.6 eV. Curve fitting and background subtraction were accomplished. The Pt-MoO_3-RGO HNRAs were also characterized by Raman spectroscopy (*Renishaw inVia)* and Fourier transform infrared spectroscopy (FTIR, Nicolet 330).

Electrochemical Characterization: The electrochemical performance of the fabricated electrocatalysts were investigated in a standard three-electrode electrolytic cell. The Pt-MoO_3-RGO HNRAs grown on Ti

substrate served as working electrode. A Pt foil served as the counter electrode. A SCE was utilized as the reference electrode. All potentials utilized in this study were the values *vs* SCE. Cyclic voltammetry (CV) and chronoamperometry measurements were carried out on a CHI 760D electrochemical workstation (CH instruments, Inc.). Before electrochemical measurements, the surface of the electrocatalyst was covered by 4.5 μL Nafion (5 wt%) solution. CV curves for methanol oxidation were recorded between -0.20 and 1.00 V *vs* SCE at 50 $mV \cdot s^{-1}$. Chronoamperometry curves for methanol oxidation were recorded at 0.60 V *vs* SCE. An aqueous solution of 0.5 M CH_3OH +0.5 M H_2SO_4 was utilized for CV and chronoamperometry measurements, and the solution was purged with high purity Ar gas for 10 min prior to all of the above experiments. The electrochemical measurements all were carried out at 25 ^{0}C.

3. Results and Discussion

The details of the fabrication of Pt-MoO_3-RGO hybrid HNRAs are described in the Experimental Section in supporting information. The typical scanning electron microscopy (SEM) image of the fabricated Pt-MoO_3-RGO hybrid HNRAs is shown in Figure 1a, which shows the diameters are ~300 nm and the lengths are ~1.5 μm. A magnified SEM image of a broken Pt-MoO_3-RGO hollow nanorod is shown in the inset in Figure 1a, and the hollow structure is clearly seen. The structure of the Pt-MoO_3-RGO hollow nanorods is further characterized by transmission electron microscopy (TEM), and the typical TEM image is shown in Figure 1b, which shows the wall thickness is homogeneous and is ~30 nm. The inner diameter is 200~300 nm. The magnified TEM image of the walls of Pt-MoO_3-RGO HNRAs is shown in Figure 1c, which shows that the Pt nanocrystals and amorphous MoO_3 uniformly disperse on RGO sheets. The sizes of Pt nanocrystals are 3~5 nm. Figure 1d shows the high resolution TEM image of Pt-MoO_3-RGO HNRAs. The lattice fringes of Pt nanocrystals are clearly seen, and the lattice spacing is determined to be 0.224 nm, which corresponds to (111) planar spacing of Pt. The HRTEM image also shows the sizes of Pt nanocrystals are 3~5 nm. The lattice fringes of MoO_3 and RGO are not seen, indicating the amorphous structure of MoO_3 and RGO. The compositions of Pt-MoO_3-RGO HNRAs were studied by energy dispersive X-ray (EDX), and the mass ratio of Pt : MoO_3 : RGO is 15 : 45 : 40 (15 wt%

Pt, Pt loading is 98.5 μg/cm^2). To investigate the distribution states of Pt, MoO_3 and RGO in the sample, EDS mapping was measured on the end tip of a broken Pt-MoO_3-RGO hollow nanorod (Figure S3) and the results are shown in Figure 1e-h, which shows the elements of Pt, Mo, O and C are uniformly dispersed, indicating high dispersive Pt, MoO_3 and RGO in the Pt-MoO_3-RGO HNRAs. High dispersive Pt nanoscrystals are also proved by the HRTEM image shown in Figure S4. Therefore, based on the above results, we successfully fabricated Pt-MoO_3-RGO ternary hybrid HNRAs with low-content of Pt (15 wt%) and high dispersive Pt, MoO_3 and RGO.

XPS spectra of the Pt-MoO_3-RGO HNRAs and Pt HNRAs in Pt 4*f* regions were shown in Figure 2a-b. For Pt HNRAs, it is clearly seen that the Pt 4*f* peaks all can be deconvoluted into two pairs of doublets. The Pt 4*f* peaks at 71.3 and 72.5 eV are assigned to Pt^0 and Pt^{II}, respectively. A comparison of the relative areas of integrated intensity of Pt^0 and Pt^{II} shows that plentiful Pt exists as Pt^{II} in the Pt HNRAs, while almost no Pt^{II} is observed in the Pt-MoO_3-RGO HNRAs, indicating that the introduction of MoO_3 and RGO can significantly increase the relative content of Pt^0 in the Pt-MoO_3-RGO HNRAs. In addition, Figure 2a shows that the Pt $4f_{7/2}$ and $4f_{5/2}$ peaks of Pt-MoO_3-RGO HNRAs both shift to lower binding energies (70.95 and 74.31 eV) relative to those of Pt HNRAs (71.31 and 74.67 eV), and this can be attributed to the strong electronic interactions that originate from the special heterogeneous interfaces among the Pt nanocrystals, MoO_3 and RGO in the Pt-MoO_3-RGO HNRAs. Figure 2c-d shows XPS spectra of Pt-MoO_3-RGO HNRAs and MoO_3 HNRAs in Mo 3d regions. For Pt-MoO_3-RGO HNRAs, the Mo $3d_{5/2}$ and $3d_{3/2}$ peaks at 232.65 and 235.81 eV, respectively, are well assigned to Mo^{6+}, indicating the existence of MoO_3 in the composites. The Mo $3d_{5/2}$ and $3d_{3/2}$ peaks of the Pt-MoO_3-RGO HNRAs both shift to higher binding energies compared with those of MoO_3 HNRAs (232.51 and 235.67 eV), indicating that the MoO_3 in Pt-MoO_3-RGO HNRAs takes part in synergistic effects among the Pt nanocrystals, MoO_3, and RGO. Figure 2e-f shows XPS spectra of the Pt-MoO_3-RGO HNRAs and RGO in C 1s regions. For Pt-MoO_3-RGO HNRAs, the symmetric C 1s peak at 284.64 eV is clearly seen for C-C bonds, demonstrating the existence of RGO. Additionally, the oxygen functionalities attached to the carbons show deconvoluted peaks for C-O (285.48 eV) and C=O (288.92 eV) at higher binding energies, indicating the existence of

small amounts of oxygenated carbon species in the RGO. The atomic ratio of C/O ratio represents the degree of reduction. On the basis of previous reports, the C/O ratio for hydrazine reduced GO is 3.62,[30] and here the C/O ratio for electroreduced GO is 3.67. Both reduction methods yield similar C/O ratios, with electroreduced GO having a slightly higher C/O ratio. So this result indicates that the electroreduction method is a feasible method for the fabrication of RGO. Figure 2e also shows the C-C peak of Pt-MoO_3-RGO HNRAs shift to lower binding energies (0.13 eV) relative to that of RGO HNRAs, suggesting that the RGO in Pt-MoO_3-RGO HNRAs also takes part in electron interactions among Pt nanocrystals, MoO_3, and RGO. Therefore, the strong electron interactions involving Pt, MoO_3, and RGO in Pt-MoO_3-RGO HNRAs are well demonstrated by the shifts of binding energies of Pt, Mo, and C, and the changed electronic states of Pt will probably improve electrocatalytic activity and durability of catalysts.

Raman spectrum shown in Figure 2g exhibit the characteristic D and G bands of RGO in the Pt-MoO_3-RGO HNRAs at 1321 and 1603 cm^{-1}, respectively. The G band can provide information on in plane vibrations of sp^2 bonded carbon, and the D band is a common feature for sp^3 defects in carbon.[31-32] The calculated I_D/I_G ratio of Pt-MoO_3-RGO hybrid HNRAs is 1.13, while that of RGO HNRAs is 0.78 as shown in Figure 2h. The increase in the I_D/I_G ratio is a clear indication of the decrease in the number of graphene layers and a higher density of defects.[33] Therefore, the RGO in Pt-MoO_3-RGO HNRAs have thinner graphene layers and higher defect density. In addition, it has been previously reported that an increase in the I_D/I_G ratio also can be attributed to the fragmentation of sp^2 domains,[34] and accordingly the increasing of I_D/I_G ratio of the Pt-MoO_3-RGO HNRAs may be attributed to the strong electron interactions among the RGO, MoO_3 and Pt nanocrystals that possibly lead to the fragmentation of sp^2 domains. In addition, the D band of Pt-MoO_3-RGO HNRAs red shift by ~34 cm^{-1} relative to that of RGO HNRAs, which also demonstrates the strong electron interactions among the RGO, MoO_3 and Pt nanocrystals. Therefore, the change of I_D/I_G ratio and red shift of D band also provide clear evidence for the presence of graphene and the strong electron interactions among Pt nanocrystals, RGO, and MoO_3 in Pt-MoO_3-RGO HNRAs. In addition, Fourier transform IR spectroscopy (FT-IR) spectra of the Pt-MoO_3-RGO HNRAs also prove the existence of RGO and electron interactions among Pt, MoO_3, and RGO as shown in Figure S5.

The advantages of the Pt-MoO_3-RGO hybrid HNRAs as electrocatalyts are shown in Scheme 1. Firstly, the high dispersive Pt, MoO_3, and RGO in the hybrid HNRAs provide rich heterogeneous interfaces, which will be very beneficial to enhance the synergistic effect among Pt, MoO_3 and RGO and subsequently can promote electrocatalytic activity of the catalysts for methanol electrooxidation. Secondly, the large open space among the neighboring nanorods and hollow structures of nanorods in Pt-MoO_3-RGO HNRAs will provide three-dimensional (3D) space for transmission of reactant and resultant molecules throughout the catalyst, and accordingly the active species can easily diffuse into the inside of catalysts and the inner catalysts will efficiently participate in electrocatalytic reactions. Thirdly, the HNRAs own excellent frame construction and can well resist the Ostwald ripening and coalescence of Pt nanocrystals and accordingly will promote electrocatalytic activity and durability of catalysts. In addition, the existence of RGO in the composites can well overcome the poor electrical conductivity of MoO_3 because of high conductivity of RGO, and accordingly the Pt-MoO_3-RGO hybrid HNRAs as electrocatalysts will own advisable electrical conductivity to promote methanol oxidation reactions commendably.

The electrochemical properties of Pt-MoO_3-RGO HNRAs electrocatalysts were firstly evaluated by the electrochemically active surface area (ECSA) that is an important parameter for the assessment of electrochemically active sites of catalysts. Cyclic voltammetry measurements of the Pt-MoO_3-RGO HNRAs, Pt-MoO_3 HNRAs (Figure S6) and commercial Pt/C catalysts (JM, Figure S7) were performed in N_2-purged 0.5 M H_2SO_4 solution at 50 mV/s and cyclic voltammograms (CVs) are shown in Figure 3a. The ECSA of catalysts can be calculated by following equation: $ECSA=Q_H/(0.21\times W_{Pt})$, where W_{Pt} represents the Pt loading (mg) in electrode, Q_H represents the charge for H-desorption (mC/cm^2), and 0.21 represents the charge required to oxidize a monolayer of H_2 on clean Pt. The ECSA of Pt-MoO_3-RGO HNRAs is calculated to be 71.20 $m^2\cdot(g, Pt)^{-1}$, which is much higher than those of commercial Pt/C catalysts(52.89 $m^2\cdot(g,Pt)^{-1}$) and Pt-MoO_3 HNRAs (34.23 $m^2\cdot(g, Pt)^{-1}$). The above results indicate that the Pt-MoO_3-RGO HNRAs can effectively enhance ECSA because of the hollow nanorod arrays, high dispersive Pt nanocrystals, and strong electron interactions among the RGO, MoO_3 and Pt nanocrystals.

To evaluate the electrocatalytic activity of the Pt-MoO_3-RGO HNRAs, cyclic voltammetry experim-

ents of Pt-MoO_3-RGO HNRAs, Pt-MoO_3 HNRAs and commercial Pt/C catalysts were carried out in solution of 0.5 M CH_3OH+0.5 M H_2SO_4, and the representative CVs are shown in Figure 3b. It is clearly seen that the specific peak current density of Pt-MoO_3-RGO HNRAs (809.5 mA mg^{-1}) is ~2.4 times higher than that of Pt-MoO_3 HNRAs (340 mA mg^{-1}) and ~2.0 times higher than that of Pt/C catalysts (400 mA mg^{-1}) (here the current densities all are normalized to the mass loading of Pt), indicating that the Pt-MoO_3-RGO HNRAs have a much higher catalytic activity towards methanol electrooxidation than the Pt-MoO_3 HNRAs and Pt/C catalysts. In addition, the electrocalytic activity of Pt-MoO_3-RGO is compared with other state-of-art electrocatalysts. The mass current densities of other Pt-based electrocatalysts are summarized in Table S1, which shows that the Pt-MoO_3-RGO HNRAs catalysts exhibit high electro-catalytic activity. The much enhanced electrocatalytic activity of Pt-MoO_3-RGO HNRAs can be mainly ascribed to much larger ECSA and the synergetic effects among the Pt, MoO_3 and RGO. In addition, when the current densities all are normalized to the ECSAs of catalysts, the Pt-MoO_3-RGO HNRAs show ~3.9 and ~5.3 times higher catalytic activity than Pt-MoO_3 HNRAs and Pt/C catalysts, respectively, as shown in Figure S8.

Chronoamperometry curve of the Pt-MoO_3-RGO HNRAs was measured in solution of 0.5 M H_2SO_4 +0.5 M CH_3OH to evaluate the rate of surface poisoning (The potential was held at 0.60 V *vs*. SCE), and the result is compared with those of the Pt-MoO_3 HNRAs and commercial Pt/C catalysts as shown in Figure 3c. It is obvious that the Pt-MoO_3-RGO HNRAs catalysts exhibit a slower current decay over time in comparison with Pt-MoO_3 HNRAs and Pt/C catalyst, indicating a higher tolerance to the carbonaceous species generated during methanol oxidation. In addition, the Pt-MoO_3-RGO HNRAs exhibit much higher current densities than Pt-MoO_3 HNRAs and Pt/C catalysts, indicating that the Pt-MoO_3-RGO HNRAs own much higher catalytic activity for methanol electrooxidation. To further demonstrate the high durability of Pt-MoO_3-RGO HNRAs, we also performed the multiturn potential cycling test. CVs of the Pt-MoO_3-RGO HNRAs with 200 cycles in solution of 0.5 M H_2SO_4+0.5 M CH_3OH at 50 mV/s are shown in Figure 3d, and the corresponding changes of the forward peak current densities with cycle increasing are shown in the inset in Figure 3d. The catalytic activity of Pt-MoO_3-RGO HNRAs drastically increases during the

initial cycles and the stable peak current density appears at ~50th cycle. After 200 cycles, the peak current density almost remains stable, indicating high cycle stability of the Pt-MoO_3-RGO HNRAs for methanol electrooxidation. The Pt-MoO_3-RGO HNRAs still keep the original morphology well after 200 cycles as shown in Figure S9.

Here we also evaluate the ability of CO antipoisoning of Pt-MoO_3-RGO HNRAs. High-purity CO gas was bubbled into 0.5 M H_2SO_4 solution for 15 min while keeping the electrode potential at 0 V to achieve maximum coverage of CO at the Pt centers. The dissolved CO was then purged out of the electrolyte by bubbling high purity Ar gas for 20 min. Two consecutive CVs were recorded for the catalysts between -0.2 and 1.0 V at 50 mV/s, and the results are shown in Figure 4a. The hydrogen desorption region disappears in the initial forward scan because of the adsorbed CO on Pt surfaces, and a large CO oxidation peak is seen on Pt-MoO_3-RGO HNRAs, indicating large ECSA of the Pt-MoO_3-RGO HNRAs. After CO_{ads} stripping, the adsorption/desorption peak of hydrogen is clearly seen and the CO_{ads} stripping peak disappears in the second scan, indicating that the complete oxidation of CO_{ads} during the 1st cycle. Therefore, the Pt-MoO_3-RGO HNRAs can facilitate removal of CO_{ads} from their surfaces. In addition, the disappearance of CO_{ads} oxidation peak after stripping indicates that the Pt-MoO_3-RGO HNRAs are free of dissolved CO. We also studied CO oxidation on the Pt-MoO_3 HNRAs and Pt/C catalysts as shown in Figure 4b and 4c, respectively. Compared with the results in Figure 4b-c, the Pt-MoO_3-RGO HNRAs show much higher peak current density of CO_{ads} oxidation than Pt-MoO_3 HNRAs and Pt/C catalysts as shown in Figure 4a. In addition, the onset peak potential (0.45 V) of CO oxidation on Pt-MoO_3-RGO HNRAs is more negative than those on Pt-MoO_3 HNRAs (0.48 V) and Pt/C catalyst (0.58 V) during CO_{ads} stripping. Therefore, the Pt-MoO_3-RGO HNRAs own higher CO oxidation ability than Pt-MoO_3 HNRAs and Pt/C catalysts. This may be attributed to high dispersive Pt nanocrystals and abundant Pt-MoO_3-RGO three-phase interfaces. As we all know, the abundant heterogeneous interfaces will lead to the formation of a large number of labile OH species,[35] which will easily exert electronic effect to the adjacent intermediate species absorbed on Pt surfaces to produce CO_2, and consequently to achieve clean Pt surfaces because of the removal of poisoning intermediate species. After CO_{ads} stripping, the Pt-MoO_3-

RGO hybrid HNRAs also show larger ECSA than Pt-MoO_3 HNRAs and Pt/C catalysts as shown in Figure 4d.

4. Conclusions

In conclusion, we have designed and fabricated the novel Pt-MoO_3-RGO hybrid HNRAs catalysts for methanol electrooxidation. Besides the strong points of HNRAs including hollow nanostructures, high utilization ratio and fast mass transport, the hybrid Pt-MoO_3-RGO HNRAs allow for strong electron interactions among Pt, MoO_3 and RGO, which results in electron delocalization among Pt 4*f* orbitals, Mo 3*d* orbitals and RGO π-conjugated ligands and accordingly high electroactive Pt. The Pt-MoO_3-RGO hybrid HNRAs also own rich heterogeneous interfaces for catalytic reactions because of high dispersive MoO_3, RGO and Pt nanocrystals and significantly improve the relative content of Pt(0) in products. The Pt-MoO_3-RGO HNRAs exhibit much higher ECSA (71.20 $m^2 \cdot (g,Pt)^{-1}$) than Pt-MoO_3 HNRAs (34.23 $m^2 \cdot (g,Pt)^{-1}$) and commercial Pt/C catalyst (52.89 $m^2 \cdot (g, Pt)^{-1}$). The experimental results demonstrate that the Pt-MoO_3-RGO HNRAs own significantly enhanced catalytic activity and durability for methanol electrooxidation compared with the Pt-MoO_3 HNRAs, commercial Pt/C and many other reported Pt-based catalysts. Our current study suggests the possibilities for design of novel catalysts with superior electrocatalytic activity and durability by the combination of compositionally and geometrically favorable factors.

Supporting Information

SEM images, IR spectra, and CVs. This material is available free of charge via the Internet at http://pubs.rsc.org.

Acknowledgements

This work was supported by National Natural Science Foundation of China (51173212), National Basic Research Program of China (2015CB932304), Natural Science Foundation of Guangdong Province (S2013020012833), Fundamental Research Fund for the Central Universities (13lgpy51), SRF for ROCS, SEM ([2012)1707), Project of High Level Talents in Higher School of Guangdong Province, Science and

Technology Planning Project of Guangdong Province (2013B010403011) and Open-End Fund of Key Laboratory of Functional Inorganic Material Chemistry (Heilongjiang University), Ministry of Education.

References

(1) (a) M.-R. Gao, Q. Gao, J. Jiang, C.-H. Cui, W.-T. Yao and S.-H. Yu, *Angew. Chem. Int. Ed.,* 2011, **50**, 4905; (b) L.-X. Ding, A.-L. Wang, G.-R. Li, Z.-Q. Liu, W. Zhao, C.-Y. Su and Y.-X. Tong, *J. Am. Chem. Soc.,* 2012, **134**, 5730.

(2) (a) H.-H. Li, S. Zhao, M. Gong, C.-H. Cui, D. He, H.-W. Liang, L. Wu and S.-H. Yu, *Angew. Chem. Int. Ed.,* 2013, **52**, 7472; (b) L. Wang and Y. Yamauchi, *J. Am. Chem. Soc.,* 2013, **135**, 16762; (c) C. Koenigsmann and S. S. Wong, *ACS Catal.,* 2013, **3**, 2031.

(3) (a) H. Yang, J. Zhang, K. Sun, S. Zou and J. Fang, *Angew. Chem. Int. Ed.,* 2010, **49**, 6848; (b) H. Wang, S. Ishihara, K. Ariga and Y. Yamauchi, *J. Am. Chem. Soc.,* 2012, **134**, 10819; (c) A. Mohanty, N. Garg and R. Jin, *Angew. Chem. Int. Ed.,* 2010, **49**, 4962.

(4) (a) Y. Liang, Y. Li, H. Wang and H. Dai, *J. Am. Chem. Soc.,* 2013, **135**, 2013; (b) J. Wu, L. Qi, H. You, A. Gross, J. Li and H. Yang, *J. Am. Chem. Soc.,* 2012, **134**, 11880; (c) H. Wang, S. Ishihara, K. Ariga and Y. Yamauchi, *J. Am. Chem. Soc.,* 2012, **134**, 10819.

(5) (a) Z. Peng and H. Yang, *J. Am. Chem. Soc.,* 2009, **131**, 7542; (b) B. Y. Xia, H. B. Wu, X. Wang and X. W. Lou, *Angew. Chem. Int. Ed.,* 2013, **52**, 12337; (c) Y. Xia, T. Ng, H. Wu, X. Wang and X. W. Lou, *Angew. Chem. Int. Ed.,* 2012, **51**, 7213.

(6) (a) K. Gong, D. Su and R. R. Adzic, *J. Am. Chem. Soc.,* 2010, **132**, 14364; (b) T. Ghosh, M. B. Vukmirovic, F. J. DiSalvo and R. R. Adzic, *J. Am. Chem. Soc.,* 2010, **132**, 906.

(7) (a) H. Wang, Y. Liang, Y. Li and H. Dai, *Angew. Chem. Int. Ed.,* 2011, **50**, 10969; (b) K. Sasaki, H. Naohara, Y. Cai, Y. M. Choi, P. Liu, M. Vukmirovic, J. X. Wang and R. R. Adzic, *Angew. Chem. Int. Ed.,* 2010, **49**, 8602.

(8) (a) F. Cheng, T. Zhang, Y. Zhang, J. Du, X. Han and J. Chen, *Angew. Chem. Int. Ed.,* 2013, **52**, 2474-2477; (b) B. Y. Xia, H. B. Wu, Y. Yan, X. W. Lou and X. Wang, *J. Am. Chem. Soc.,* 2013, **135**, 9480; (c) X. Zhao, M. Yin, L. Ma, L. Liang, C. Liu, J. Liao, T. Lu and W. Xing, *Energy Environ. Sci.,* 2011, **4**, 2736.

(9) (a) A. Yin, X.-Q. Min, Y.-W. Zhang and C.-H. Yan, *J. Am. Chem. Soc.,* 2011, **133**, 3816; (b) H. Ataee-Esfahani, M. Imura and Y. Yamauchi, *Angew. Chem. Int. Ed.,* 2013, **52**, 13611.

(10) (a) L. Wang, Y. Nemoto and Y. Yamauchi, *J. Am. Chem. Soc.,* 2011, **133**, 9674; (b) C. Li, T. Sato and Y. Yamauchi, *Angew. Chem. Int. Ed.,* 2013, **52**, 8050.

(11) (a) J. Suntivich, Z. Xu, C. E. Carlton, J. Kim, B. Han, S. W. Lee, N. Bonnet, N. Marzari, L. F. Allard, H. Gasteiger, K. Hamad-Schifferli and Y. Shao-Horn, *J. Am. Chem. Soc.,* 2013, **135**, 7985; (b) B. Xia, H. Wu, X. Wang and X. W. Lou, *J. Am. Chem. Soc.,* 2012, **134**, 1393.

(12) (a) L. Zhang, N. Li, F. Gao, L. Hou and Z. Xu, *J. Am. Chem. Soc.,* 2012, **134**, 11326; (b) S. W. Lee, S. Chen, W. Sheng, N. Yabuuchi, Y.-T. Kim, T. Mitani, E. Vescovo and Y. Shao-Horn, *J. Am. Chem. Soc.,* 2009, **131**, 15669.

(13) (a) L. Liu, E. Pippel, R. Scholz and U. Gösele, *Nano Lett.,* 2009, **9**, 4352. (b) M. Gong, G. Fu, Y. Chen, Y. Tang and T. Lu, *ACS Appl. Mater. Interfaces,* 2014, **6**, 7301-7308. (c) G. Fu, K. Wu, J. Lin, Y. Tang, Y. Chen, Y. Zhou and T. Lu, *J. Phys. Chem. C,* 2013, **117**, 9826-9834.

(14) (a) Y. Kang, J. Pyo, X. Ye, T. R. Gordon and C. B. Murray, *ACS Nano,* 2012, **6**, 5642; (b) S. Guo, S. Dong and E. Wang, *ACS Nano,* 2010, **4**, 547.

(15) (a) J.-J. Zhang, Z.-B. Wang, C. Li, L. Zhao, J. Liu, L.-M. Zhang, and D. Gu. *J. Power Sources*., 2015, **289**, 63-70. (b) L. Zhao, Z.-B. Wang, J. Liu, J.-J. Zhang, X.-L. Sui, L.-M. Zhang and D. Gu. *J. Power Sources*., 2015, **279**, 210-217.

(16) X. Han, F. Cheng, T. Zhang, J. Yang, Y. Hu and J. Chen, *Adv. Mater.,* 2014, **26**, 2047.

(17) Y. Shiraishi, H. Sakamoto, Y. Sugano, S. Ichikawa and T. Hirai, *ACS Nano,* 2013, **7**, 9287.

(18) M. Tian, G. Wu and A. Chen, *ACS Catal.,* 2012, **2**, 425.

(19) Y. Liu, S. Shrestha and W. E. Mustain, *ACS Catal.,* 2012, **2**, 456.

(20) J. Xie, X. Yang, B. Han, Y. Shao-Horn and D. Wang, *ACS Nano,* 2013, **7**, 6337.

(21) Z. Liu, J. E. Hu, Q. Wang, K. Gaskell, A. Frenkel, G. Jackson and B. Eichhorn, *J. Am. Chem. Soc.,* 2009, **131**, 6924.

(22) M. Liu, R. Zhang and W. Chen, *Chem. Rev.,* 2014, DOI: 10.1021/cr400523y.

(23) Y. Li, Y. Li, E. Zhu, T. McLouth, C.-Y. Chiu, X. Huang and Y. Huang, *J. Am. Chem. Soc.,* 2012, **134**, 12326.

(24) (a) Y. Qu, Y. Gao, F. Kong, S. Zhang, L. Du and G. Yin, *Int. J. Hydrogen Energy,* 2013, **38**, 12310; (b) C. Wang, F. Jiang, R. Yue, H. Wang and Y. Du, *J. Solid State Electrochem.,* 2014, **18**, 515.

(25) (a) S. Guo, S. Zhang, D. Su and S. Sun, *J. Am. Chem. Soc.,* 2013, **135**, 13879; (b) H.-X. Liu, N. Tian, M. P. Brandon, Z.-Y. Zhou, J.-L. Lin, C. Hardacre, W. -F. Lin and S.-G. Sun, *ACS Catal.,* 2012, **2**, 708.

(26) Q.-S. Chen, Z.-Y. Zhou, F. J. Vidal-Iglesias, J. Solla-Gullón, J. M. Feliu and S.-G. Sun, *J. Am. Chem. Soc.,* 2011, **133**, 12930.

(27) S. Jiang, Y. Ma, G. Jian, H. Tao, X. Wang, Y. Fan, Y. Lu, Z. Hu and Y. Chen, *Adv. Mater.,* 2009, **21**, 4953.

(28) H.-H. Li, C.-H. Cui, S. Zhao, H.-B. Yao, M.-R. Gao, F.-J. Fan and S.-H. Yu, *Adv. Energy Mater.,* 2012, **2**, 1182.

(29) S. Guo, S. Dong and E. Wang, *Energy Environ. Sci.,* 2010, **3**, 1307.

(30) S. D. Perera, R. G. Mariano, K. Vu, N. Nour, O. Seitz, Y. Chabal and K. J. Balkus, Jr. *ACS Catal.,* 2012, **2**, 949.

(31) R. Rao, R. Podila, R. Tsuchikawa, J. Katoch, D. Tishler, A. Rao and M. Ishigami, *ACS Nano,* 2011, **5**, 1594.

(32) K. Kudin, B. Ozbas, H. Schniepp, R. Prud'homme, I. Aksay and R. Car, *Nano Lett.,* 2008, **8**, 36.

(33) I. Yoon, C.-D. Kim, B.-K. Min, Y.-K. Kim, B. Kim and W.-S. Jung, *Bull. Korean Chem. Soc.* **2009**, *30*, 3045.

(34) (a) J. Shen, B. Yan, M. Shi, H. Ma, N. Li and M. Ye, *J. Mater. Chem.,* 2011, **21**, 3415; (b) K. Zhou, Y. Zhu, X. Yang, X. Jiang and C. Li, *New J. Chem.,* 2011, **35**, 353.

(35) J. Zeng, J. Yand, J. Lee and W. Zhou, *J. Phys. Chem. B,* 2006, **110**, 24606.

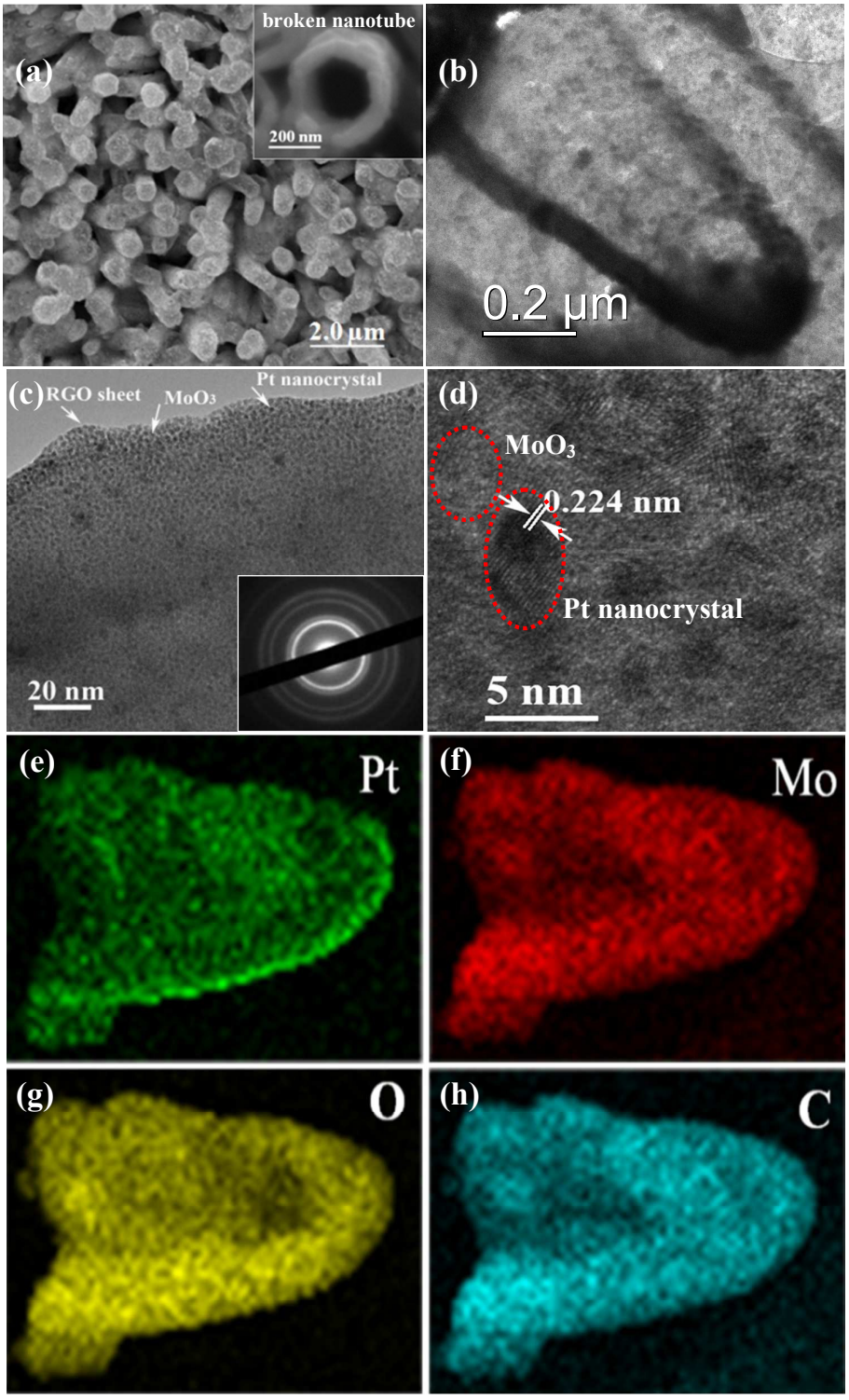

Figure 1. (a) SEM; (b) TEM; (c) high-magnified TEM; and (d) HRTEM images (SAED) of Pt-MoO_3-RGO HNRAs. EDS mappings measured on the end tip of a Pt-MoO_3-RGO hollow nanorod: (e) Pt, (f) Mo, (g) O and (h) C elements.

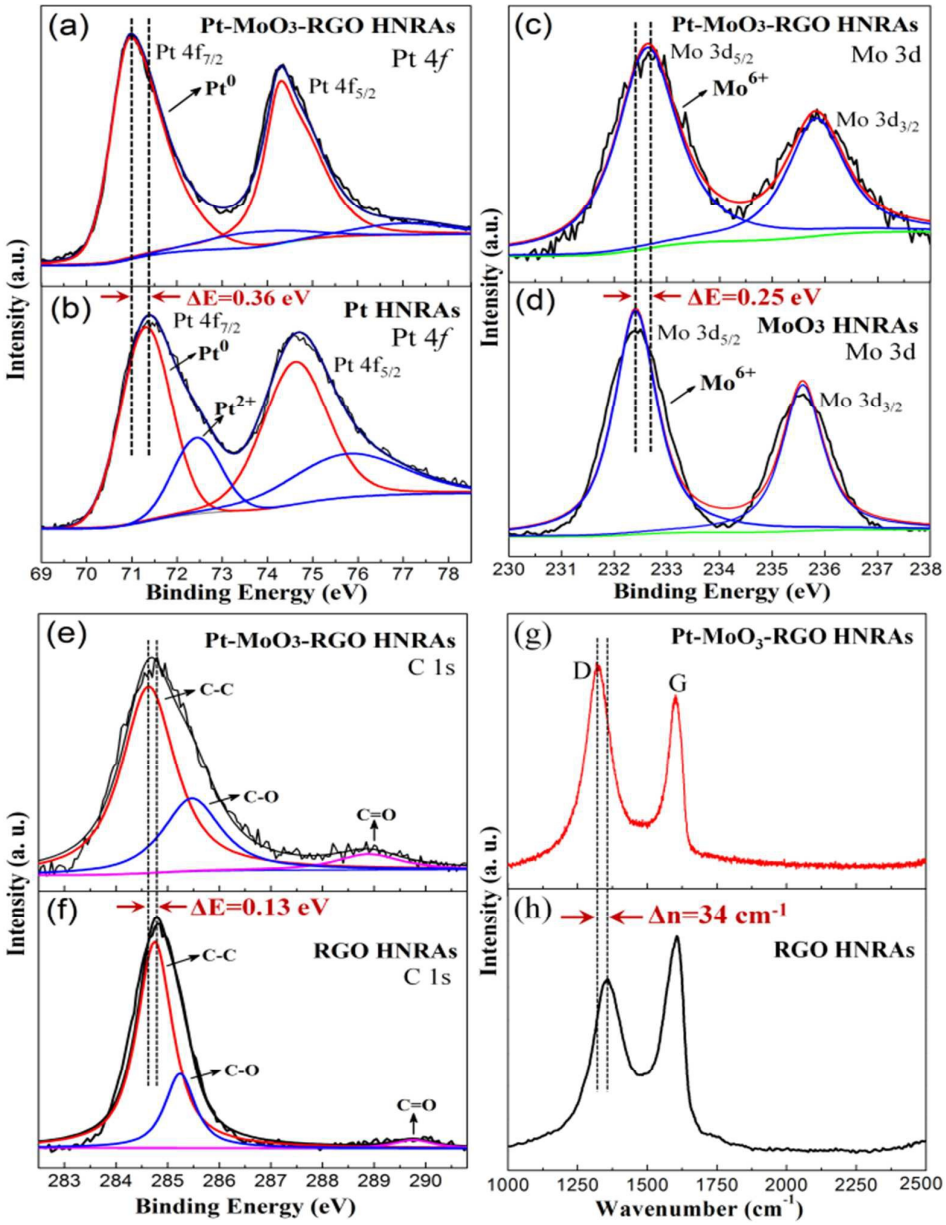

Figure 2. XPS spectra of Pt *4f* performed on (a) Pt-MoO_3-RGO HNRAs and (b) Pt HNRAs; XPS spectra of Mo 3d performed on (c) Pt-MoO_3-RGO HNRAs and (d) MoO_3 HNRAs; XPS spectra of C1s performed on (e) Pt-MoO_3-RGO HNRAs and (f) RGO HNRAs; Raman spectra measured on (g) Pt-MoO_3-RGO HNRAs and (h) RGO HNRAs.

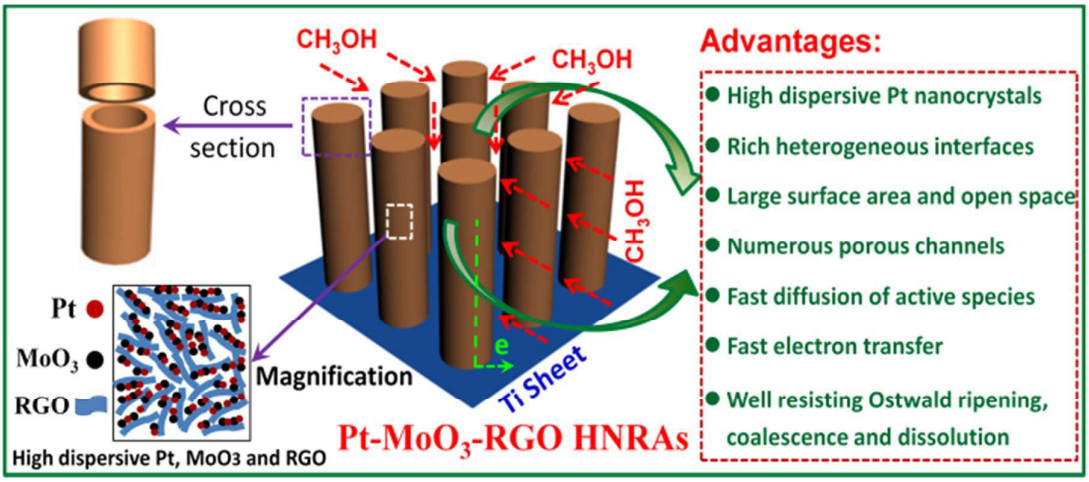

Scheme 1. Schematic illustration for the advantages of Pt-MoO_3-RGO HNRAs as electrocatalysts.

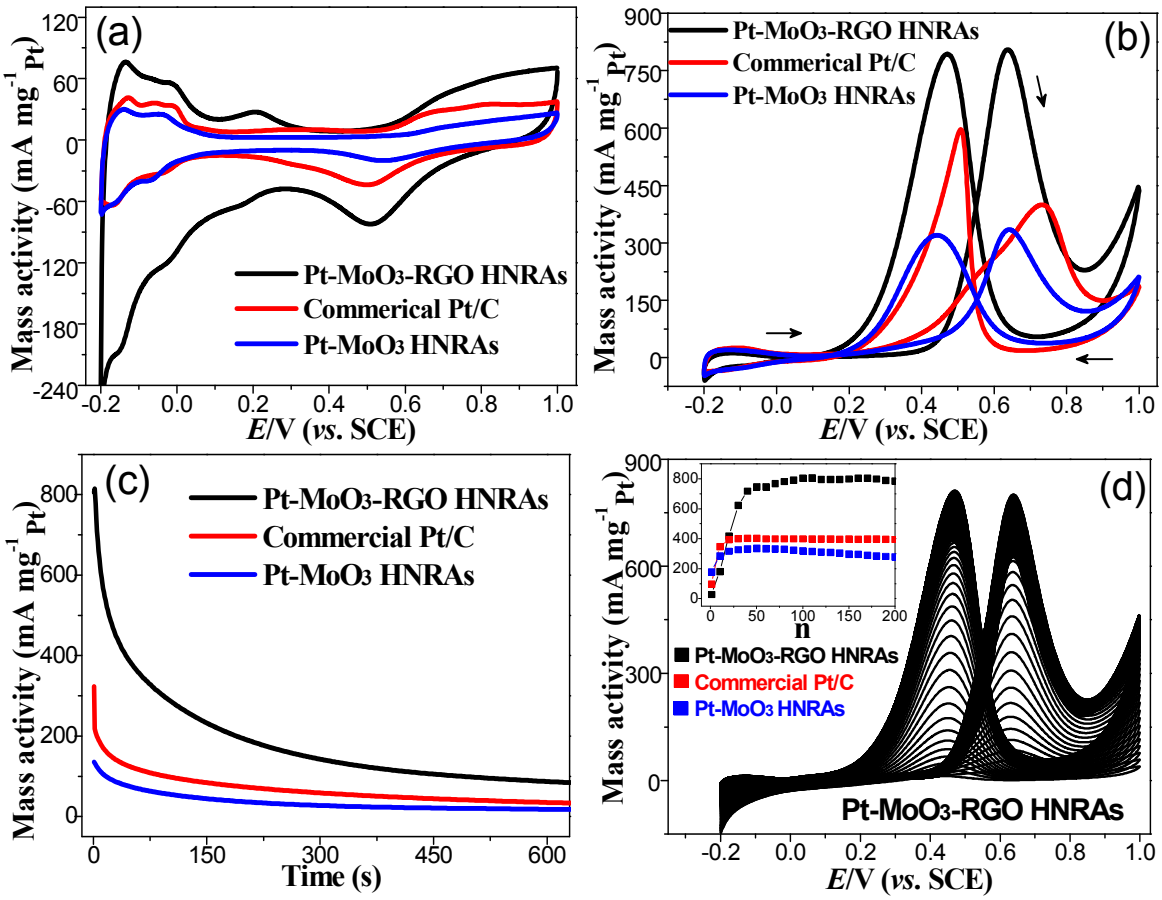

Figure 3. (a) CVs measured in 0.5 M H_2SO_4 solution at 50 mV/s; (b) CVs measured in 0.5 M CH_3OH+0.5 M H_2SO_4 solution at 50 mV/s; (c) Chronoamperometry curves measured in solution of 0.5 M H_2SO_4 +0.5 M CH_3OH at 50 mV/s (The corresponding potential was held at 0.60 V); (d) CVs of Pt-MoO_3-RGO HNRAs from 1st to 200th cycle (Inset shows the change of peak current density of forward peak with cycle increasing for the Pt-MoO_3-RGO HNRAs, Pt-MoO_3 HNRAs, and commercial Pt/C catalysts)

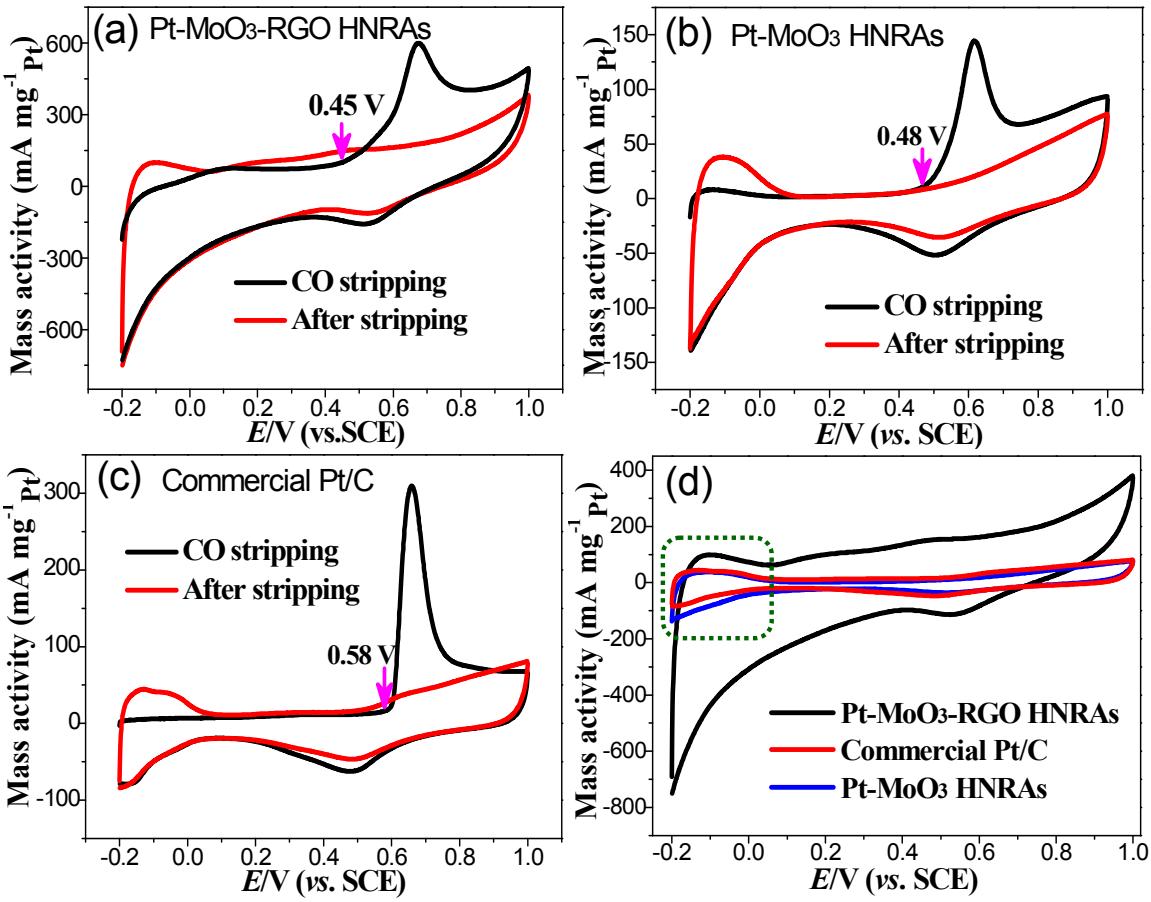

Figure 4. CO stripping CVs on (a) Pt-MoO_3-RGO HNRAs; (b) Pt-MoO_3 HNRAs; and (c) commercial Pt/C catalysts performed in solution of 0.5 M H_2SO_4 at 50 mV/s at room temperature; (d) The comparisons of CVs after CO stripping on the Pt-MoO_3-RGO HNRAs, Pt-MoO_3 HNRAs and commercial Pt/C catalysts.

The table of contents entry

Pt-MoO_3-RGO Ternary Hybrid Hollow Nanorod Arrays as High-Performance Catalysts for Methanol Electrooxidation

An-Liang Wang, Han Xu, Jin-Xian Feng, Ye-Xiang Tong, and Gao-Ren Li*